

# **Part I**

## **State of the Mantle: Properties and Dynamic Evolution**

# Long-Wavelength Mantle Structure: Geophysical Constraints and Dynamical Models

Maxwell L. Rudolph<sup>1</sup>, Diogo L. Lourenço<sup>1</sup>, Pritwiraj Moulik<sup>2</sup>, and Vedran Lekić<sup>2</sup>

## ABSTRACT

The viscosity of the mantle affects every aspect of the thermal and compositional evolution of Earth's interior. Radial variations in viscosity can affect the sinking of slabs, the morphology of plumes, and the rate of convective heat transport and thermal evolution. Below the mantle transition zone, we detect changes in the long-wavelength pattern of lateral heterogeneity in global tomographic models, a peak in the the depth-distribution of seismic scatterers, and changes in the dynamics plumes and slabs, which may be associated with a change in viscosity. We analyze the long-wavelength structures, radial correlation functions, and spectra of four recent global tomographic models and a suite of geodynamic models. We find that the depth-variations of the spectral slope in tomographic models are most consistent with a geodynamic model that contains both a dynamically significant phase transition and a reduced-viscosity region at the top of the lower mantle. We present new inferences of the mantle radial viscosity profile that are consistent with the presence of such a feature.

## 1.1. INTRODUCTION

Heterogeneity in Earth's mantle is dominated by its very long-wavelength components in the upper mantle, transition zone, and the lowermost mantle. Such long-wavelength variations reflect the distribution of the continents and the ocean basins in the uppermost mantle, subducted slabs in the transition zone and the degree-2 dominant continent-sized large low shear velocity provinces (LLSVPs) in the lowermost mantle. The long-wavelength structure of the upper mantle is positively correlated with the lowermost mantle structure (Figure 1.1),

supporting the well-established idea that the lower mantle and lithospheric plate systems mutually interact through subduction and upwelling to produce related large-scale structures. However, the transition zone and shallow lower mantle contain large-scale heterogeneity that is weakly anticorrelated with the upper mantle and lowermost mantle. Observations of deflected upwellings, slab stagnation above and below the 650 km phase transition, the presence of seismic scatterers, and changes in the large-scale pattern of mantle structure suggest the possibility of changes in mantle properties across this region that lack a single agreed-upon explanation.

The presence of faster-than-average material surrounding the pair of LLSVPs in the lowermost mantle can be explained well by models of slab sinking constrained by subduction history, assuming that slabs sink vertically from the trench (Ricard et al., 1993), even when using only the most recent 200 Myr of subduction history. Although

<sup>1</sup>Department of Earth and Planetary Sciences, University of California, Davis, CA, USA

<sup>2</sup>Department of Geology, University of Maryland, College Park, MD, USA

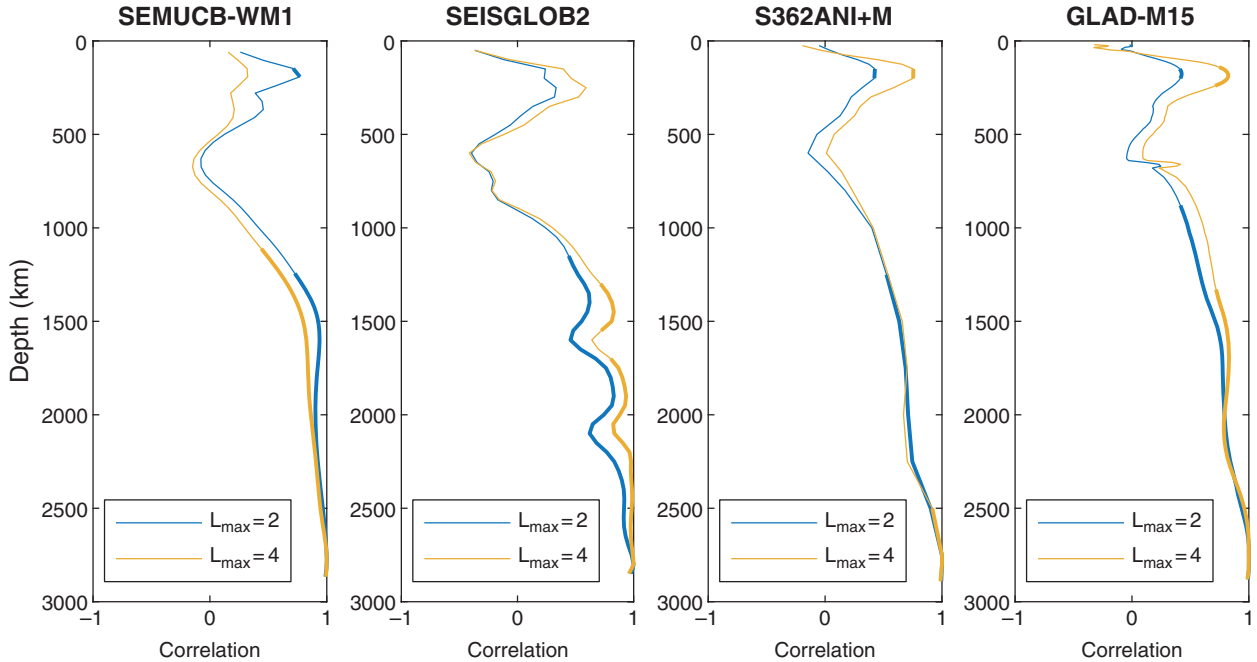


**Figure 1.1** Correlation between structure at 2800 km depth and other mantle depths for each of four tomographic models. Correlations for spherical harmonic degrees 1–2 are shown in blue and degrees 1–4 are shown in yellow. Where the curves are thicker, the correlation is significant at the  $p = 0.05$  level.

the thermochemical nature of LLSVPs is sometimes debated (e.g., Davies et al., 2015), several lines of evidence now suggest that the LLSVPs are both warmer and compositionally distinct from the surrounding lower mantle. The anti-correlation of shear- and bulk sound speed (Su and Dziewonski, 1997; Masters et al., 2000), sharp boundaries imaged by detailed waveform modeling (e.g., He and Wen, 2009; Wang and Wen, 2007), tidal constraints (Lau et al., 2017), and inferences of density from full-spectrum tomography (e.g., Moulik and Ekström, 2016) are all consistent with a thermochemical rather than purely thermal origin of the LLSVPs. Additional evidence for a thermochemical origin is provided by the distribution of present day hotspots near the interiors and margins of the LLSVPs (Thorne et al., 2004; Burke et al., 2008; Austermann et al., 2014), expected on the basis of laboratory analogue experiments and numerical simulations (Davaille et al., 2002; Jellinek and Manga, 2002), as well as the observation that primitive helium isotope ratios in ocean island basalts are associated with mantle plumes rooted in the LLSVPs (e.g., Williams et al., 2019). The reconstructed eruption locations of large igneous provinces also fall near the present-day boundaries of the LLSVPs (Burke and Torsvik, 2004; Torsvik et al., 2006), which supports the idea that the LLSVPs have been relatively stable over at least the past 200 Myr. Geodynamic models that impose time-dependent, paleogeographically constrained plate motions can produce

chemical piles whose large-scale features are consistent with the morphology of the LLSVPs (e.g., McNamara and Zhong, 2005; Bower et al., 2013; Rudolph and Zhong, 2014).

All recent global tomographic models are generally in very good agreement at long wavelengths in the lowermost mantle (e.g., Becker and Boschi, 2002; Cottaar and Lekic, 2016). The long-wavelength structure, comprising spherical harmonic degrees 1–4, is consistent in the upper and lowermost mantle across four recent global  $V_S$  tomographic models (Figure 1.2). However, shear velocity variations across the mantle transition zone and shallow lower mantle appear to shift to a pattern that is weakly anticorrelated with structure in both the asthenosphere and lowermost mantle. This change in large-scale structure, evident in the global maps of  $V_S$  variations (Figure 1.2), is also captured by the mantle radial correlation function (RCF), shown in Figure 1.3 (e.g., Jordan et al., 1993; Puster and Jordan, 1994), which measures the similarity of the pattern of structures between every pair of depths in the mantle. Radial correlation analyses of global tomographic models reveal a zone of decorrelation across the transition zone and shallow lower mantle. Some (but not all) recent global shear-wave (e.g., French and Romanowicz, 2014; Durand et al., 2017) and P wave (Fukao and Obayashi, 2013; Obayashi et al., 2013) tomographic models show a dramatic change in the radial correlation structure near

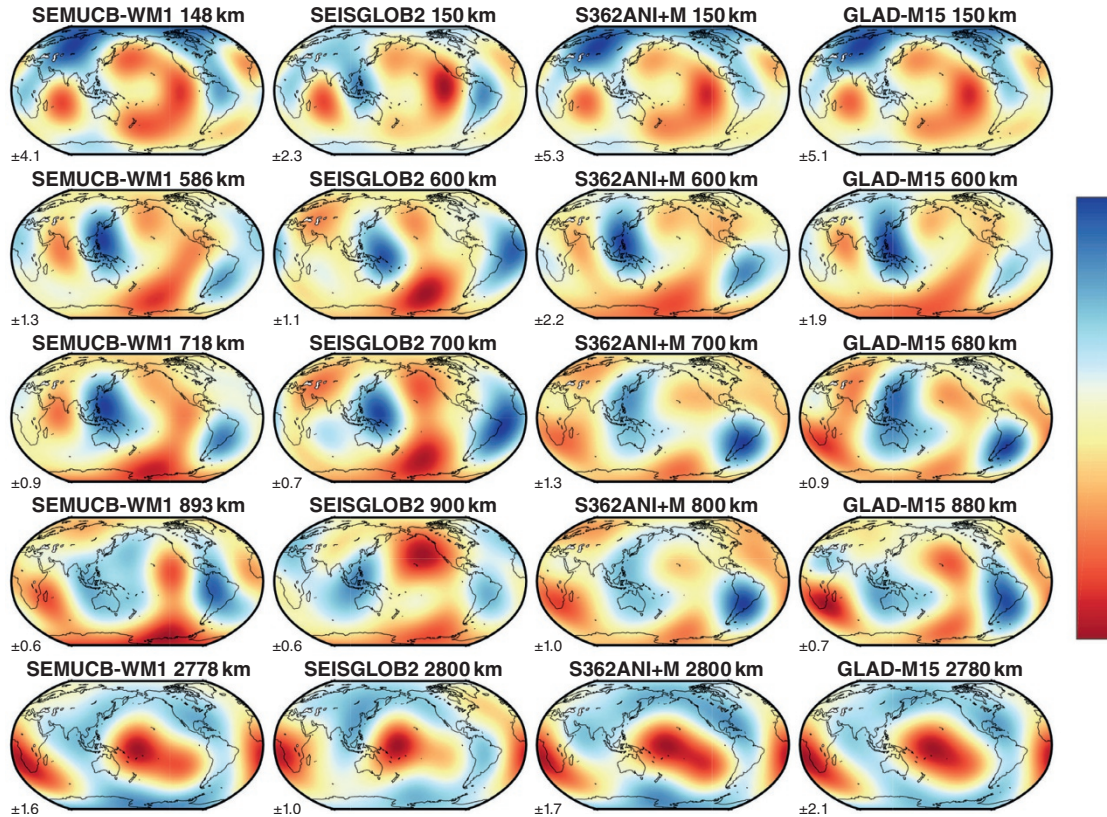


**Figure 1.2** Shown here are plots of Voigt  $V_S$  variations at spherical harmonic degrees 1–4 from four recent tomographic models at selected depths across the transition zone and shallow lower mantle and within the lowermost mantle and the lithosphere. In each subpanel, the amplitude of the color scale is indicated in percent.

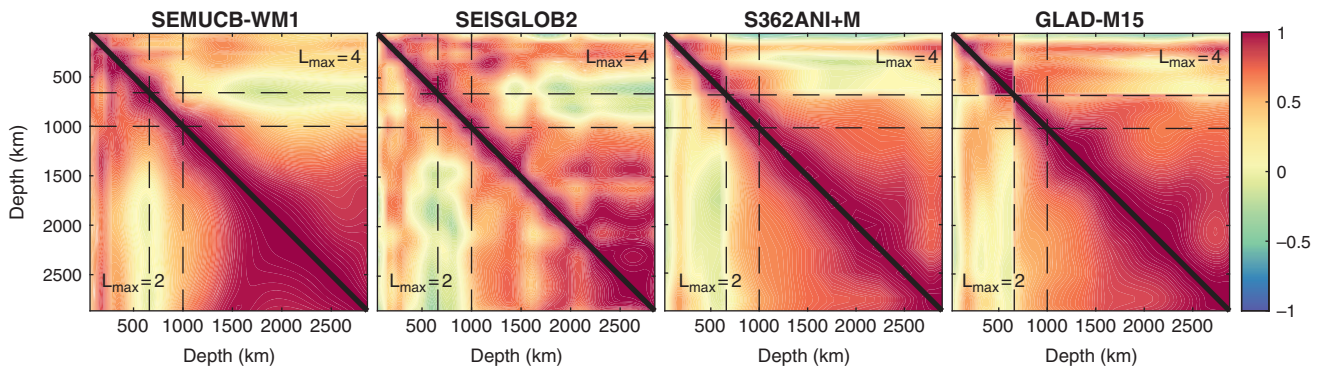


**Figure 1.3** Radial correlation functions computed for four recent global tomographic models. The color scale indicates the value of the correlation between structures at different mantle depths. In each panel, the lower-left triangle is the RCF for only spherical harmonic degrees 1–2, while the upper right triangle shows the RCF for degrees 1–4.

1,000 km depth. While the precise depth of the change in the long-wavelength correlation is affected by the data constraints and model parameterization choices of the tomographic models (discussed later), it appears to coincide with other shorter-wavelength features such as

scatterers and deflected plumes, suggesting that they may share a common dynamical origin.

Changes in the continuity and shape of upwelling and downwelling features have been identified in both global and regional tomographic models. The

whole-mantle waveform tomographic model SEMUCB-WM1 (French and Romanowicz, 2014) reveals striking lateral deflections of upwellings beneath several active hotspots. In particular, the imaged plume conduit beneath St. Helena appears to be deflected 1,000–650 km, in contrast to its more vertical shape in the lower mantle below 1,000 km and in the upper mantle and transition zone (French and Romanowicz, 2015). While St. Helena provides perhaps the most striking example, there are also possible deflections near 1,000 km beneath the Canaries and Macdonald (French and Romanowicz, 2015). Regional tomography of the North Atlantic shows some evidence of deflection of the Iceland plume above 1,000 km depth (Rickers et al., 2013), though this is not seen in all regional and global models (French and Romanowicz, 2015; Yuan and Romanowicz, 2017). Regional tomography indicates that the Yellowstone plume is laterally shifted near 1,000 km (Nelson and Grand, 2018). Slabs imaged in the global  $P$  wave model GAP-P4 (Obayashi et al., 2013; Fukao and Obayashi, 2013) appear to stagnate within or below the mantle transition zone. The Northern Mariana slab is imaged as a nearly horizontal feature above 1,000 km, the Java slab is stagnant or less steeply inclined above 1,000 km, and the Tonga slab is imaged as a horizontal fast anomaly above 1,000 km (Fukao and Obayashi, 2013). This behavior is not universal; in Central America, there is no evidence for slab ponding or stagnation, and many slabs in the Western Pacific and South America are imaged above 650 km depth.

Seismic scatterers have been identified in the mid-mantle, and their depth-distribution peaks near 1,000 km. Using  $P$ -to- $S$  receiver function stacks, Jenkins et al. (2016) located scatterers beneath Europe, Iceland, and Greenland. The scatterers are distributed at depths of  $\sim$ 800–1400 km, with a peak near 1,000 km. In global surveys of seismic reflectors, scatterers are observed in all regions with data coverage, and with no clear association to tectonic province or subduction history (Waszek et al., 2018; Frost et al., 2018). The global distribution of reflectors imaged by Waszek et al. (2018) is quite broadly distributed across the depth range of 850–1300 km with a peak close to 875 km depth. Changes in the distribution of small-scale heterogeneity are also supported by analyses of the spectra of tomographic models. A decrease in the redness in mantle tomographic models occurs below 650 km, coincident with the observations of short-wavelength scattering features, stagnant slabs, and deflected upwellings.

The observational evidence for changes in mantle structure from long-wavelength radial correlation, the behavior of upwellings and downwellings, and the depth- and lateral-distribution of short wavelength scattering features suggests the possibility of changes in mantle

properties and processes in the mid mantle. Several mechanisms have been proposed for such a change, including a change in viscosity (Rudolph et al., 2015) or a change in composition (Ballmer et al., 2015). In the remainder of this chapter, we present new analyses of mantle tomographic models with an eye toward understanding which features in the tomographic models give rise to the changes in the long-wavelength radial correlation structure. Next, we use 3D spherical geometry mantle convection models to assess the implications of different mantle viscosity structures for the development of large-scale structure. Finally, we examine previous and new inferences of the mantle viscosity profile, constrained by the long-wavelength geoid.

## 1.2. METHODS

### 1.2.1. Mantle Tomography

We compare the results of the geodynamic modeling with the characteristics of four recent global tomographic  $V_S$  models that differ in data selection, theoretical framework, and model parameterization and regularization choices. SEMUCB-WM1 (French and Romanowicz, 2014) is a global anisotropic shear-wave tomographic model based on full-waveform inversion of three-component long-period seismograms, divided into wave-packets containing body waves and surface waves including overtones. Accurate waveform forward modeling is achieved using the spectral element method (Capdeville et al., 2005), 2D finite frequency kernels are computed using nonlinear asymptotic coupling theory (Li and Romanowicz, 1995), and the tomographic model is constructed by iterating using the quasi-Newton method. SEISGLOB2 (Durand et al., 2017) is an isotropic shear-wave model constrained by data sensitive primarily to  $V_{SV}$  structure—spheroidal mode splitting functions, Rayleigh wave phase velocity maps, and body wave travel-times. The inverse problem is fully linearized, with sensitivity of normal mode and Rayleigh wave data computed using first order normal mode perturbation theory, and traveltimes data using ray theory, both computed in a reference spherically symmetric model. GLAD-M15 (Bozdağ et al., 2016) is a global tomographic model that, like SEMUCB-WM1, aims to fit full, three-component seismic waveforms. Once again, the spectral element method (Komatitsch and Tromp, 2002) enables accurate forward modeling, while 3D finite frequency kernels are computed using the adjoint method at each iteration. GLAD-M15 uses S362ANI (Kustowski et al., 2008) as a starting model and carries out an iterative conjugate gradient refinement of the 3D velocity structure to match observations while accounting for the full nonlinearity

of the sensitivity of the misfit function to earth structure. The fourth model, S362ANI+M (Moulik and Ekström, 2014), is a global model based on full-spectrum tomography, which employs seismic waveforms and derived measurements of body waves ( $\sim 1$ –20s), surface waves (Love and Rayleigh,  $\sim 20$ –300s), and normal modes ( $\sim 250$ –3300s) to constrain physical properties – seismic velocity, anisotropy, density, and the topography of discontinuities – at variable spatial resolution. The inverse problem is solved iteratively and jointly with seismic source mechanisms, using sensitivity kernels that account for finite-frequency effects for the long-period normal modes, along-branch coupling for waveforms and ray theory for body-wave travel times and surface-wave dispersion. Model SEISGLOB2 was obtained as spatial expansions of Voigt  $V_S$  in netcdf format from the IRIS Data Management Center ([http://ds.iris.edu/ds/products/emc-earthmodels/](http://ds.iris.edu/ds/products/emc-earthmodels/http://ds.iris.edu/ds/products/emc-earthmodels/)). S362ANI+M was provided in netcdf format on a two-degree grid and at 25 depths. GLAD-M15 was provided on a degree-by-degree grid and at 132 depths by the authors (Bozdağ, *pers. comm.*). Model SEMUCB-WM1 was obtained from the authors’ web page and evaluated using the model evaluation tool a3d on a degree-by-degree grid at 65 depths.

The tomographic models were expanded into spherical harmonics to calculate power spectra and to facilitate wavelength-dependent comparisons among models. First, at each depth, models were resampled using linear interpolation onto 40,962 equispaced nodes, providing a uniform resolution equivalent to  $1 \times 1$  equatorial degree. Spherical harmonic expansions were carried out using the *slepian* MATLAB routines (Simons et al., 2006). Spherical harmonic coefficients were computed using the  $4\pi$ -normalized convention, such that the spherical harmonic basis functions  $Y_{lm}$  satisfy  $\int_{\Omega} Y_{lm} Y_{l'm'} d\Omega = 4\pi \delta_{ll'} \delta_{mm'}$  where  $\Omega$  is the unit sphere. The power per degree and per unit area  $\sigma_l^2$  was computed as

$$\sigma_l^2 = \sum_{m=0}^{l_{\max}} (a_{lm}^2 + b_{lm}^2), \quad (1.1)$$

where  $a_{lm}$  and  $b_{lm}$  are real spherical harmonic coefficients (and  $b_{l0} = 0$  for all  $l$ ). We note that Equation (1.1) is a measure of power per unit area per spherical harmonic degree, and not per spherical harmonic coefficient. This choice differs by a factor of  $1/(2l+1)$  from the definitions adopted in Dahlen and Tromp (1998) and used in Becker and Boschi (2002), and our definition omitting the multiplicative prefactor gives the appearance of a flatter power spectrum. Because we use this convention uniformly here, the choice of convention for the normalization of power does not affect our interpretations. From the spherical harmonic power spectra, we computed a spectral slope,

which contains information about the relative amounts of power present at different wavelengths. Multiple definitions of spectral slope have been used with spherical harmonic functions, depending on whether spectral fitting is carried out in log-log or log-linear space. Here, the spectral slope is defined based on a straight-line fit to  $\sigma_l^2$  vs.  $l$  in log-log coordinates, for spherical harmonic degrees 2–20. A slope of zero would indicate uniform power at all spherical harmonic degrees (the power spectrum of a delta function on the sphere (e.g., Dahlen and Tromp, 1998)), and increasingly negative slopes indicate more rapidly decreasing power at shorter wavelengths.

Radial correlation functions (Jordan et al., 1993; Puster and Jordan, 1994; Puster et al., 1995) were calculated from the spherical harmonic expansions. The RCF measures the similarity of  $\delta_V$  structures at depths  $z$  and  $z'$  as

$$R_{\delta_V}(z, z') = \frac{\int_{\Omega} \delta_V(z, \theta, \phi) \delta_V(z', \theta, \phi) d\Omega}{\sqrt{\int_{\Omega} \delta_V(z, \theta, \phi)^2 d\Omega} \sqrt{\int_{\Omega} \delta_V(z', \theta, \phi)^2 d\Omega}}. \quad (1.2)$$

where  $\theta$  and  $\phi$  denote the polar angle and azimuthal angle and  $\Omega$  refers to integration over  $\theta$  and  $\phi$ . When working with normalized spherical harmonic functions, the above expression is equivalent to the linear correlation coefficient of vectors of spherical harmonic coefficients representing the velocity variations. Because the denominator of the expression for radial correlation normalizes by the standard deviations of the fields at both depths, the RCF is sensitive only to the pattern and not to the amplitude of velocity variations.

### 1.2.2. Mantle Circulation Models

We carried out a suite of 3D geodynamic models in spherical geometry using CitcomS version 3.1.1 (Zhong et al., 2000, 2008) with modifications to impose time-dependent plate motions as a surface boundary condition (Zhang et al., 2010). CitcomS solves the equations of mass, momentum, and energy conservation for incompressible creeping (zero Reynolds number) flow under the Boussinesq approximation in 3D spherical shell geometry. All of the models include a compositionally distinct layer (advected using tracers), meant to be analogous to the LLSVP material, which is assigned an excess density of 3.75%, equivalent to a buoyancy ratio of  $B = 0.5$ . The intrinsic density difference adopted here is chosen such that the compositionally distinct material remains stable against entrainment and is consistent with other geodynamic modeling studies (Mc-Namara and Zhong, 2004, 2005), leading to a net buoyancy compatible with the available constraints from normal modes and solid earth tides Moulik and Ekström (2016); Lau et al. (2017). The compositionally distinct material is initially

present as a uniform layer of 250 km thickness. All of the models include time-dependent prescribed surface plate motions, which shape the large-scale structure of mantle flow. We adopt plate motions from a recent paleogeographic reconstruction by Matthews et al. (2016), which spans 410 Ma-present, although some of the calculations do not include the entire plate motion history. All of the models except Case 40 (Table 1.1) impose the initial plate motions for a period of 150 Myr to spin-up the model and initialize large-scale structure following Zhang et al. (2010). The mechanical boundary conditions at the core-mantle boundary are free-slip, and the temperature boundary conditions are isothermal with a nondimensional temperature of 0 at the surface and 1 at the core-mantle boundary. We use a temperature- and depth-dependent viscosity with the form  $\eta(z) = \eta_z(z) \exp[E(0.5 - T)]$ , where  $\eta_z(z)$  is a depth-dependent viscosity prefactor and  $E = 9.21$  is a dimensionless activation energy, which gives rise to relative viscosity variations of  $10^4$  due to temperature variations. The models are heated by a combination of basal and internal heating, with a dimensionless internal heating rate  $Q = 100$ .

We include the effects of a phase transition at 660 km depth in some of the models. Phase transitions are implemented in CitcomS using a phase function approach (Christensen and Yuen, 1985). We adopt a density increase across 660 km of 8%, a reference depth of 660 km, a reference temperature of 1573 K, and a phase change width of 40 km. We assume a Clapeyron slope of  $-2$  MPa/K. Recent experimental work favors a range of  $-2$  to  $-0.4$  MPa/K (Fei et al., 2004; Katsura et al., 2003), considerably less negative than values employed in earlier geodynamical modeling studies that produced layered convection (Christensen and Yuen, 1985). The models shown in the present work are a subset of a more exhaustive suite of models from Lourenço and Rudolph (in review), which consider a broader range of convective vigor and additional viscosity structures. We list the parameters that are varied between the five models in Table 1.1 and the radial viscosity profiles used in all of the models are shown in Figure 1.4.

### 1.2.3. Inversions for Viscosity

We carried out inversions for the mantle viscosity profile constrained by the long-wavelength nonhydrostatic geoid. The amplitude and sign of geoid anomalies depend on the internal mantle buoyancy structure as well as the deflection of the free surface and core-mantle boundary, which, in turn, are sensitive to the relative viscosity variations with depth (Richards and Hager, 1984; Hager et al., 1985). Because the long-wavelength geoid is not very sensitive to lateral viscosity variations (e.g., Richards and Hager, 1989; Ghosh et al., 2010), we neglect these, solving only for the radial viscosity profile. The geoid is not sensitive to absolute variations in viscosity, so the profiles determined here show only relative variations in viscosity, and absolute viscosities could be constrained using a joint inversion that includes additional constraints such as those offered by observations related to glacial isostatic adjustment. In order to estimate the viscosity profile, we first convert buoyancy anomalies from mantle tomographic models into density anomalies and then carry out a forward model to generate model geoid coefficients. We then compare the modeled and observed geoids using the Mahalanobis distance

$$\Phi(\underline{m}) = (\underline{N}_{\text{model}}(\underline{m}) - \underline{N}_{\text{obs}})^{\top} \underline{C}_D^{-1} (\underline{N}_{\text{model}}(\underline{m}) - \underline{N}_{\text{obs}}), \quad (1.3)$$

where  $\underline{N}$  denotes a vector of geoid spherical harmonic coefficients calculated from the viscosity model with parameters  $\underline{m}$ ,  $\underline{C}_D$  is the data-plus-forward-modeling covariance matrix. The Mahalanobis distance is an  $L_2$ -norm weighted by an estimate of data+forward modeling uncertainty, and is sensitive to both the pattern and amplitude of misfit.

We used geoid coefficients from the GRACE geoid model GGM05 (Ries et al., 2016) and the hydrostatic correction from Chambat et al. (2010). We use a transdimensional, hierarchical, Bayesian approach to the inverse problem (e.g., Sambridge et al., 2013), based on the methodology described in (Rudolph et al., 2015). We carry out

**Table 1.1** Summary of parameters used in geodynamic models.  $z_{lm}$  denotes the depth of the viscosity increase between the upper and lower mantle and  $\Delta\eta_{lm}$  is the magnitude of the viscosity increase at this depth. LVC indicates whether the model includes a low-viscosity channel below 660 km. Spinup time is the duration for which the initial plate motions are imposed prior to the start of the time-dependent plate model. We indicate whether the model includes the endothermic phase transition, which always occurs at a depth of 660 km and with Clapeyron slope  $-2$  MPa/K.

Case	$z_{lm}$	$\Delta\eta_{lm}$	LVC?	Spinup time	Phase transition?	Start time
Case 8	660 km	100	No	150 Myr	No	400 Ma
Case 9	660 km	30	No	150 Myr	No	400 Ma
Case 18	1000 km	100	No	150 Myr	Yes	400 Ma
Case 32	660 km	100	No	150 Myr	Yes	400 Ma
Case 40	660 km	100	Yes	0 Myr	Yes	250 Ma

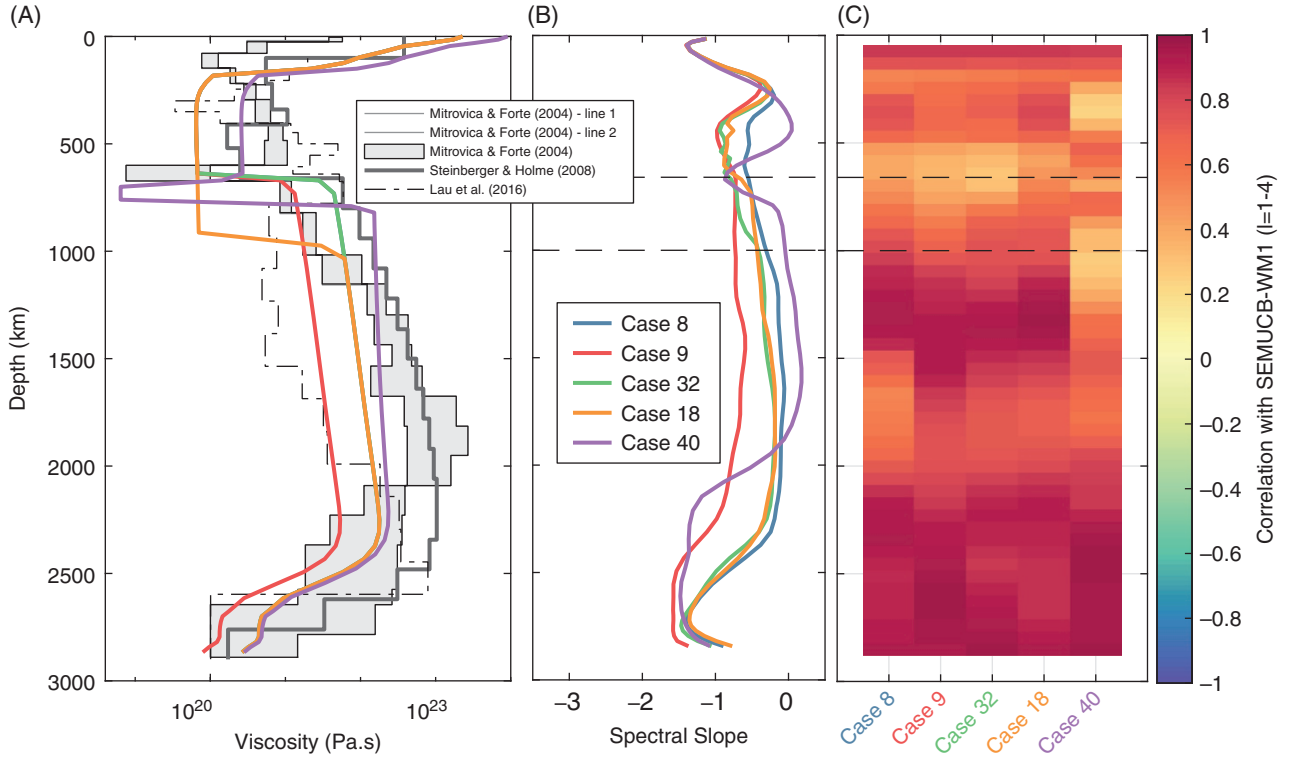


**Figure 1.4** (A) Viscosity profiles used in our geodynamic models. For comparison, we also show viscosity profiles obtained in a joint inversion constrained by glacial isostatic adjustment (GIA) and convection-related observables (Mitrovia and Forte (2004) Figure 1.4B), a combination of geoid, GIA, geodynamic constraints (Case C from Steinberger and Holme (2008)) and a joint inversion of GIA data including the Fennoscandian relaxation spectrum (Fig. 12 from Lau et al. (2016)). (B) Spectral slope vs. depth computed from the dimensionless temperature field of the geodynamic models. (C) Correlation at spherical harmonic degrees 1–4 between each of the geodynamic models and SEMUCB-WM1.

forward models of the geoid using the propagator matrix code HC (Hager and O’Connell, 1981; Becker et al., 2014). Relative to our previous related work (Rudolph et al., 2015), the inversions presented here differ in their treatment of uncertainty, scaling of velocity to density variations, and parameterization of radial viscosity variations.

We inferred density anomalies from two different tomographic models. First, we used SEMUCB-WM1 and scaled Voigt  $V_S$  anomalies to density using a depth-dependent scaling factor for a pyrolitic mantle composition along a 1600 K mantle adiabat, calculated from thermodynamic principles using HeFESTo (Stixrude and Lithgow-Bertelloni, 2011). Second, we used a whole-mantle model of density variations constrained by full-spectrum tomography (Moulik and Ekström, 2016). This model, hereafter referred to as ME16-160, imposes a best data-fitting scaling factor between density and  $V_S$  variations of  $d \ln \rho / d \ln V_S = 0.3$  throughout the mantle. We note that Moulik and Ekström (2016) present a suite of

models with different choices for data weighting and preferred correlation between density variations and  $V_S$  variations in the lowermost mantle. The specific model used here ignores sensitivity to the density-sensitive normal modes (data weight  $w_{0,S_2} = 0$ ) and imposes strong  $V_S - \rho$  correlation in the lowermost mantle ( $\gamma_{\rho}^{D''} = 10^{11}$ ). While this model is not preferred by seismic data, these choices produce a density model that closely resembles a scaled  $V_S$  model in the lowermost mantle. We note that the assumption of purely thermal contributions to density is unlikely to be correct in the lowermost mantle, where temperature and compositional variations both contribute to density variations. However, this assumption should not affect our inferences of viscosity, for two reasons. First, previous viscosity inversions found that removing all buoyancy structure from the bottom 1,000 km of the mantle did not significantly influence the retrieved viscosity profile (Rudolph et al., 2015). This is confirmed by inversions for a four-layer viscosity structure constrained by thermal vs. thermochemical mantle buoyancy (Liu and Zhong

(2016). Second, geodynamic models of thermochemical convection suggest that the thermal buoyancy above the LLSVPs counteracts the thermal and chemical buoyancy of the compositionally distinct LLSVPs, resulting in only a very small net contribution to the long-wavelength geoid from the bottom 1,000 km of the mantle (Liu and Zhong, 2015).

In the inversions using SEMUCB-WM1, we assume a diagonal covariance matrix to describe the data and forward modeling uncertainty on geoid coefficients, i.e., uncorrelated errors and uniform error variance at all spherical harmonic degrees (because the corresponding posterior covariance matrix is not available). For the inversions using ME16-160, we first sample the *a posteriori* covariance matrix of the tomographic model, generating a collection of  $10^5$  whole-mantle models of density and wavespeed variations. For each of these models, we calculate a synthetic geoid assuming a reference viscosity profile (Model C from *Steinberger and Holme (2008)*). This procedure yields a sample of synthetic geoids from which we calculate a sample covariance matrix that is used to compute the Mahalanobis distance as a measure of viscosity model misfit.

In all of the inversions shown in this chapter, we include a hierarchical hyperparameter that scales the covariance matrix. This parameter has the effect of smoothing the misfit function in model space, and the value of the hyperparameter is retrieved during the inversion, along with the other model parameters. The inversion methodology, described completely in Rudolph et al. (2015), uses a reversible-jump Markov-Chain Monte Carlo (rjMCMC) method (Green, 1995) to determine the model parameters (the depths and viscosity values of control points

describing the piecewise-linear viscosity profile) and the noise hyperparameter (Malinverno, 2002; Malinverno and Briggs, 2004). The rjMCMC method inherently includes an Occam factor, which penalizes overparameterization. Adding model parameters must be justified by a significant reduction in misfit. The result is a parsimonious parameterization of viscosity that balances data fit against model complexity. In general, incorporating additional data constraints or *a priori* information about mantle properties could lead to more complex solutions.

### 1.3. RESULTS

The power spectra of four recent global tomographic models are shown in Figure 1.5. While S362ANI+M contains little power above spherical harmonic degree 20 due to its long-wavelength lateral parameterization with 362 evenly spaced spline knots, the other models contain significant power at shorter wavelengths that are beyond the scope of this study. In general, the models are dominated by longer wavelengths at all depths. The spectral slope for each model (up to degree 20) is shown in the rightmost panel of Figure 1.5. Increasingly negative spectral slopes indicate that heterogeneity is dominated by long-wavelength features. All of the models generally show a more negative spectral slope in the transition zone than in the upper mantle or the shallow lower mantle, indicating the presence of more long-wavelength  $V_S$  heterogeneity within the transition zone and just below the 650 km discontinuity, which we attribute to the lateral deflection of slabs.

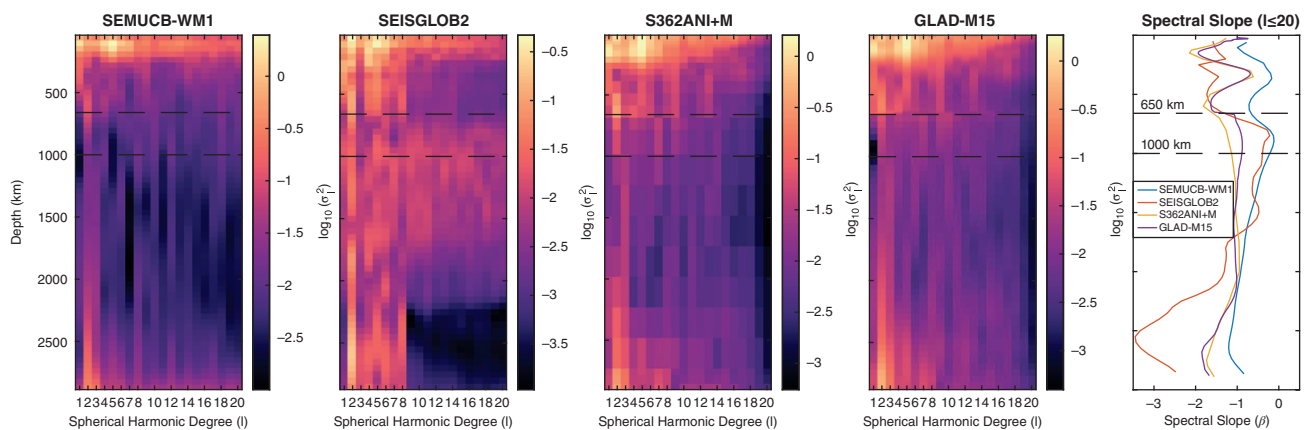


**Figure 1.5** Power spectra of four recent global  $V_S$  tomographic models. Because our focus is on long-wavelength structure, and to ensure a more equitable comparison, we show only spherical harmonic degrees 1–20, though SEMUCB-WM1, SEISGLOB2, and GLAD-M15 contain significant power at shorter wavelengths. At the right, we show spectral slopes (defined in the text) for the four models. Here, increasingly negative values indicate a concentration of power in longer wavelengths/lower spherical harmonic degrees.

Figure 1.3 shows radial correlation plots for the four tomographic models. Here, the spherical harmonic expansions are truncated at degrees 2 (lower left triangle) and 4 (upper right triangle). At degrees 1–2 and 1–4, both SEMUCB-WM1 and SEISGLOB2 show a clear change in the correlation structure near 1,000 km depth. On the other hand, S362ANI+M and GLAD-M15 both show a change in correlation structure at 650 km.

We compared the character of heterogeneity in the geodynamic models with mantle tomography by calculating the power spectrum and spectral slope of each of the five geodynamic models. Because the depth-variation of power in the geodynamic models does not have as straightforward an interpretation as the  $V_S$  power spectra shown for tomographic models, we focus on the spectral slope of the geodynamic models, shown in Figure 1.4. We computed correlation coefficients between each of the geodynamic models and SEMUCB-WM1, shown in Figure 1.4C.

For both of the tomographic models used to infer mantle viscosity, we carried out viscosity inversions (Figure 1.6) constrained by spherical harmonic degree 2 only, degrees 2 and 4 only, and degrees 2–7. The viscosity profiles are quite similar, regardless of which spherical harmonic degrees are used to constrain the inversion. However, we observe an increase in the overall

complexity of the viscosity profile as more spherical harmonic degrees are included, as well as a tendency towards developing a low-viscosity region below the 650 km discontinuity (red curves in Figure 1.6), considered in the context of parsimonious inversions, this tendency toward increased complexity can be attributed to the progressively greater information content of the data. The posterior ensembles from the viscosity inversions contain significant variability among accepted solutions, and the solid lines in Figure 1.6 indicate the log-mean value of viscosity present in the ensemble at each depth while the shaded regions enclose 90% of the posterior solutions. We note that while the individual solutions in the posterior ensemble produce an acceptable misfit to the geoid, the ensemble mean itself may not. Therefore, potential applications in the future need to account for all samples of viscosity models in our ensemble rather than employ or evaluate the ensemble mean in isolation.

#### 1.4. DISCUSSION

The recent tomographic models considered here show substantial discrepancies in the large-scale variations within the mid mantle. The low overall RMS of heterogeneity (with the consequent small contribution to data

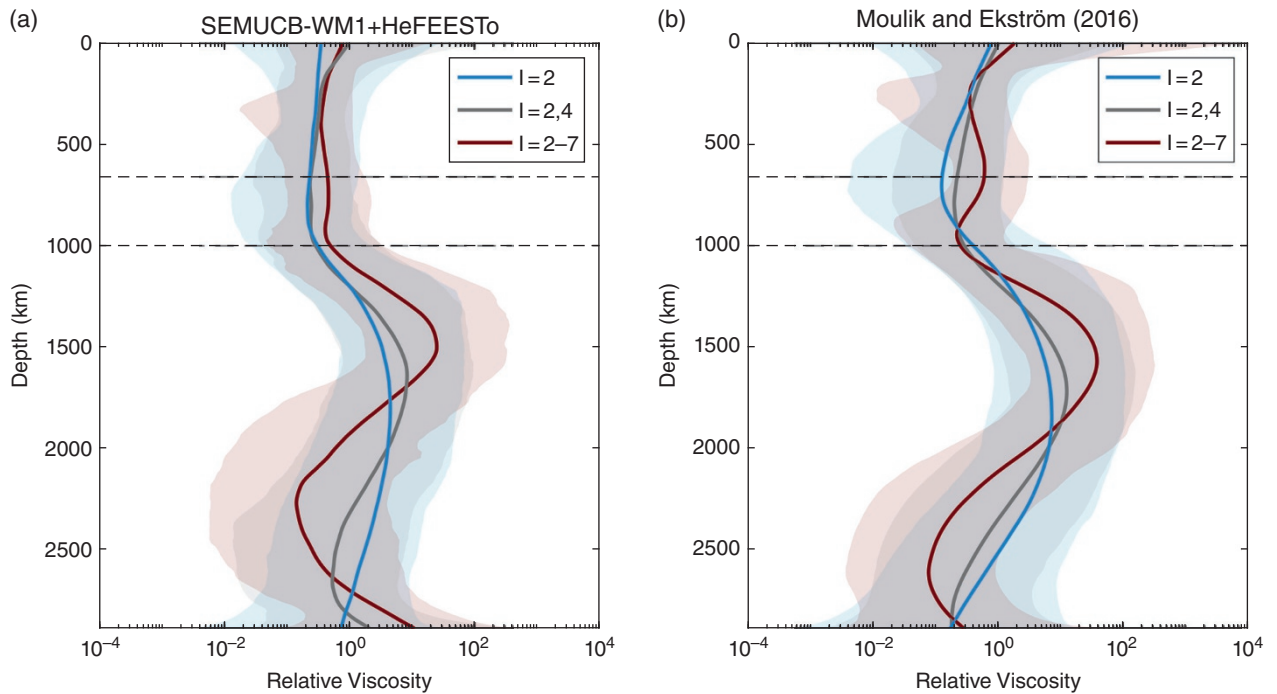


**Figure 1.6** Results from transdimensional, hierarchical, Bayesian inversions for the mantle viscosity profile, using two different models for density. (a) Density was scaled from Voigt  $V_S$  variations in SEMUCB-WM1 using a depth-dependent scaling factor computed using HeFEESTo (Stixrude and Lithgow-Bertelloni, 2011). (b) Density variations from a joint, whole-model mantle of density and seismic velocities (Moulik and Ekström, 2016)

variance) and a reduction in data constraints at these depths (e.g., normal modes, overtone waveforms) exacerbates the relative importance of *a priori* information (e.g., damping) in some tomographic models. The RCF plots shown in Figure 1.3 show that even at the very long wavelengths characterized by spherical harmonic degrees 1–2 and 1–4, there is rapid change in the RCF near 1,000 km in SEMUCB-WM1 and SEISGLOB2. On the other hand, S362ANI+M and GLAD-M15 both show more evidence for a change in structure near 1,000 km at degrees 1–2 but closer to the 650 km discontinuity for degrees up to 4. In order to understand the changes in the RCF, spatial expansions of the structures in the four tomographic models are shown for degrees 1–4 and at depths within the lithosphere, transition zone, and lowermost mantle are shown in Figure 1.2. We previously examined the long-wavelength structure of SEMUCB-WM1 and suggested that the changes in its RCF at 1,000 km depth are driven primarily by the accumulation of slabs in and below the transition zone in the Western Pacific (Lourenço and Rudolph, in review).

The shift in pattern of mantle heterogeneity within and below the transition zone is influenced by changes in the large-scale structure of plate motions. In Figure 1.7, we show the long-wavelength structure of plate motions at 0, 100, and 200 Ma. We expanded the divergence component of the plate motion model by Matthews et al. (2016) using spherical harmonics and show only the longest-wavelength components of the plate motions. This analysis is similar in concept to the multipole expansion carried out by Conrad et al. (2013) to assess the stability of long-wavelength centers of upwelling, as a proxy for the long-term stability of the LLSVPs. These long-wavelength characteristics of the plate motions need to be interpreted with some caution because the power spectrum of the divergence of plate motions is not always dominated by long-wavelength power, and power at higher degrees may locally erase some of the structure that overlaps with low spherical harmonic degrees (Rudolph and Zhong, 2013). However, for the present day (Figure 1.7, right column), the long-wavelength divergence field does show a pattern of flow with centers of long-wavelength

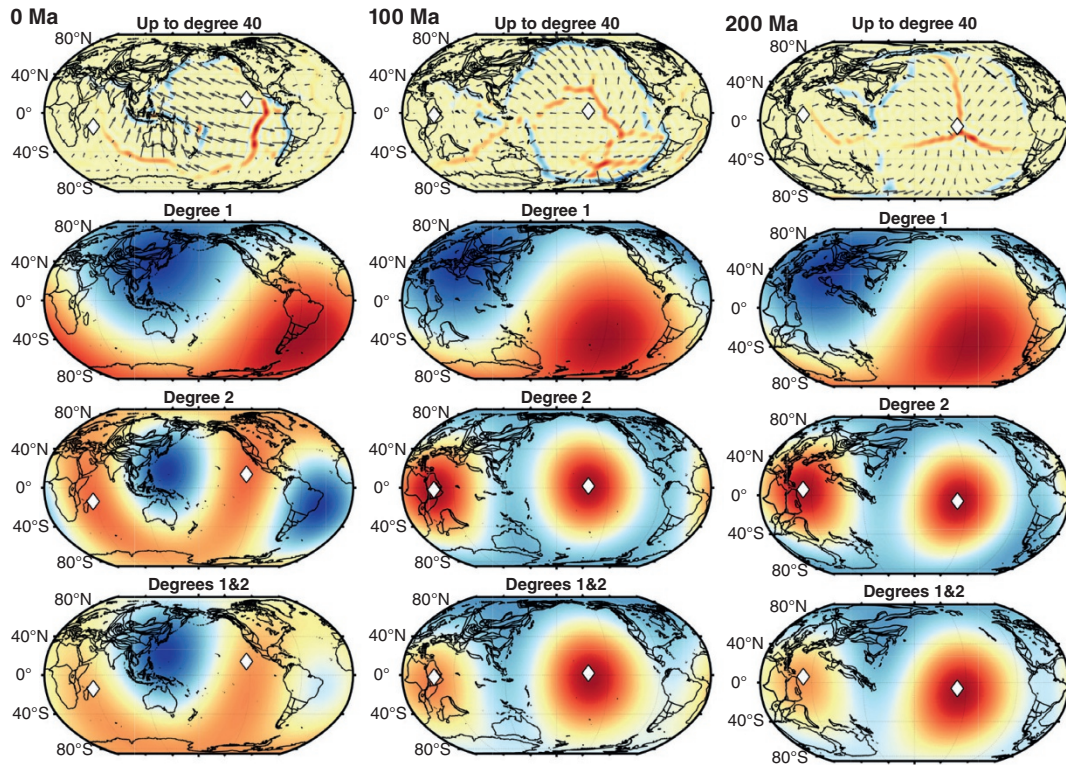


**Figure 1.7** Divergence component of plate motions computed for 0, 100, and 200 Ma. In the top row, we show the divergence field up to spherical harmonic degree 40. Red colors indicate positive divergence (spreading) while blue colors indicate convergence. The second row shows only the spherical harmonic degree-1 component of the divergence field, which represents the net motion of the plates between antipodal centers of long-wavelength convergence and divergence. The third row shows the spherical harmonic degree-2 component of the divergence, and the bottom row shows the sum of degrees 1 and 2. The white diamonds in the bottom two rows indicate the locations of the degree-2 divergence maxima (i.e., centers of degree-2 spreading).

convergence centered beneath the Western Pacific and beneath South America, where most of the net convergence is occurring. On the other hand, at 100 and 200 Ma, the pattern of long-wavelength divergence is dominated by antipodal centers of divergence, ringed by convergence. The mid-mantle structures seen in global tomographic models (Figure 1.2) closely resemble the long-wavelength divergence field for 0 Ma, while the lowermost mantle structure is most correlated with the divergence field from 100 and 200 Ma (Figure 1.7). This analysis of the long wavelength components of convergence/divergence and the long-wavelength mantle structure is consistent with analyses of the correlation between subduction history with mantle structure that include shorter wavelength structures (Wen and Anderson, 1995; Domeier et al., 2016). In particular, Domeier et al. (2016) found that the pattern of structure at 600–800 km depth is highly correlated with the pattern of subduction at 20–80 Ma. This suggests a straightforward interpretation of the changes in very long wavelength mantle structure, and the associated RCF, because the present-day convergence has a distinctly different long-wavelength pattern from the configuration of convergence at 50–100 Ma, and the mid-mantle structure is dominated by the more recently subducted material. We note, however, that this explanation addresses only the seismically fast features and does not capture additional complexity associated with active upwellings.

The power spectra of mantle tomographic models contain information about the distribution of the spatial scales of velocity heterogeneity in the mantle, and this can be compared with the power spectra of geodynamic models. Interpreting the relative amounts of power at different wavelength but at a constant depth is more straightforward than the interpretation of depth-variations in power spectral density. In mantle tomography, decreasing resolution with depth as well as the different depth-sensitivities of the seismological observations such as surface wave dispersion, body wave travel times, and normal modes used to constrain tomographic models can lead to changes in power with depth that may not be able to accurately reflect the *true* spectrum of mantle heterogeneity. The geodynamic models presented here have only two chemical components – ambient mantle and compositionally dense pile material. The models are carried out under the Boussinesq approximation, so there is no adiabatic increase in temperature with depth, and the governing equations are solved in nondimensional form. Therefore, to make a direct comparison of predicted and observed shear velocity heterogeneity, many additional assumptions are necessary to map dimensionless temperature variations into wavespeed variations. The effective value of  $d \ln V_S / d \ln T$  at constant pressure is depth-dependent, with values decreasing by more than a factor of two from

the asthenosphere to 800 km depth (e.g., Cammarano et al., 2003), and compositional effects become as important as temperature in the lowermost mantle (Karato and Karki, 2001). Here, we compare the temperature spectrum of geodynamic models with the  $\delta V_S$  spectrum in tomographic models, and this is most appropriate at depths where long-wavelength  $V_S$  variations are primarily controlled by temperature. For all of the mantle tomographic models considered, there is a local minimum in spectral slope centered on (or slightly above for SEMUCB-WM1) 650 km, reflecting the dominance of long-wavelength structures noted above. Below the base of the transition zone, the spectral slope increases, suggesting the presence of shorter-wavelength velocity heterogeneity. In the lowermost mantle, all of the tomographic models are again dominated by very long-wavelength structures, indicated by a decrease in the power spectral slope. We note that the slope for SEISGLOB2 is quite different from the other models due to the limited power at spherical harmonic degrees above 8 in this model, which may be due to regularization choices and limited sensitivity of their data to short-wavelength structure.

In analyzing the changes in spectral content of tomographic models, we assume that the model spectral content is an accurate reflection of the true spectrum of mantle heterogeneity. A geodynamic study has suggested that there could be substantial aliasing from shorter to longer wavelengths due to model regularization, limited data sensitivities and theoretical assumptions (Schuberth et al., 2009), potentially influencing our inferences of spectral slopes in the transition zone. However, aliasing is likely to be very limited at the wavelengths considered here for three reasons. First, aliasing is expected to be small if the model parameterization is truncated at a spherical harmonic degree where the power spectrum has a rapid falloff with degree (e.g., Mégnin et al., 1997; Boschi and Dziewonski, 1999). Second, a recent model like S362ANI+M uses diverse observations – normal modes, body waves (S, SS, SS precursors), long-period surface waves, and overtone waveforms – whose data variance are dominated by the longest wavelength components and show a clear falloff in power above a corner wave number (e.g., Su and Dziewonski, 1991, 1992; Masters et al., 1996). Third, we note that the spectral slope minimum in the lower part of the transition zone is recovered with models that employ various theoretical approximations.

The geodynamic models all produce long-wavelength structures that are quite similar to tomographic models at the surface and in the lowermost mantle, but there are some distinct differences in the mid-mantle that arise from differences in the viscosity profiles and inclusion or omission of phase transitions. In Figure 1.4c, we show the correlation between each of the convection models and SEMUCB-WM1 as a function of depth, for spherical

harmonic degrees 1-4. All of the models produce structures that are highly correlated with SEMUCB-WM1 in the lithosphere and and lowermost mantle. The former is entirely expected because the lithospheric temperature structure is entirely determined by plate cooling in response to the imposed plate motions, which are well-constrained for the recent past. Similar models have successfully predicted the long-wavelength lowermost mantle structure, which is shaped largely by subduction history (e.g., McNamara and Zhong, 2005; Zhang et al., 2010). Recently, Mao and Zhong (2018; 2019) demonstrated that the inclusion of an endothermic phase transition at 660 km in combination with a low viscosity channel below the transition zone can produce slab behaviors consistent with tomographically imaged structures beneath many subduction zones.

Our Case 40 includes a low-viscosity channel below 660 km and a phase transition but differs from the models shown in Mao and Zhong (2018) in that we use a longer plate motion history and a different plate reconstruction. We find that relative to the other models considered, this model produces the best correlation in long-wavelength structure within and immediately below the mantle transition zone (Figure 1.4c), but poorer overall correlation between c. 800–1,000 km than the other models considered. Intriguingly, the power spectral slope in Case 40 is more similar to the pattern seen in the tomographic models (Figure 1.5) than any of the other cases, showing an increase in the slope of the power spectrum below the base of the transition zone, similar to the feature observed in SEISGLOB2 (*Durand et al.*, 2017). The key parameter that distinguishes this model from the others is the inclusion of the low-viscosity channel, which can have a “lubrication” effect on slabs, allowing them to move laterally below the base of the transition zone. Among the other cases, we can see that there is limited sensitivity of the power spectral slope to whether viscosity is increased at 660 km or 1,000 km depth. Indeed, in Cases 18 (viscosity increase at 1,000 km) and 9 (viscosity increase at 660 km depth), the most significant change in spectral slope is at a depth of 660 km, coincident with the included phase transition. We note that Case 9 has the best overall correlation with the tomographic model due to high values of correlation throughout much of the lower mantle, but does not reproduce structure in the transition zone or shallow lower mantle as well as some of the other models.

In previous work (*Rudolph et al.*, 2015), we presented evidence for an increase in viscosity in the mid-mantle based on inversions constrained by the long-wavelength geoid. The viscosity inversions shown in Figure 1.6 are quite similar to what we found previously, despite different choices in parameterization (piecewise linear variation of viscosity vs. piecewise constant), and the use of a different tomographic model (the density model ME16-160, for

which results are shown in Figure 1.6b). There are key differences in the parameterizations of SEMUCB-WM1 versus the density model ME16-160, especially near the transition zone. SEMUCB-WM1 uses a continuous parameterization in the radial direction using splines, whereas ME16-160, which adopts the same radial parameterization as S362ANI and S362ANI+M (e.g., *Kustowski et al.*, 2008; *Moulik and Ekström*, 2014), allows a discontinuity in the parameterization at 650 km depth. Moreover, S362ANI+M includes data particularly sensitive to these depths such as normal modes and the precursors to the body wave phase *SS* that reflect off transition-zone discontinuities. As a result, the change in the pattern of heterogeneity from the transition zone to the lower mantle across the 650-km discontinuity is more abrupt in ME16-160 compared to SEMUCB-WM1. The depth and abruptness of changes in structure are exactly the features reflected in the plots of the radial correlation function in Figure 1.3. SEMUCB-WM1 shows a clear decorrelation at 1,000 km depth and a minimum in correlation length at 650 km. On the other hand, S362ANI+M and GLAD-M15 show the most substantial change in correlation structure at 650 km depth and a minimum in correlation at shallower depths in the upper mantle. Given the differences in the depths at which major changes in lateral structure occur in SEMUCB-WM1 vs. ME16-160, one might expect to recover a somewhat different preferred depth of viscosity increase between the upper mantle and lower mantle, because the preferred depth of the viscosity increase is typically very close to the crossover depth from positive to negative sensitivity in the geoid kernel. The fact that viscosity inversions with both tomographic models yield a viscosity increase substantially deeper than 650 km and closer to 1,000 km may therefore be significant.

Some of the inferred viscosity profiles contain a region with reduced viscosity below the 650 km phase transition (Figure 1.6b). The low-viscosity channel emerges as a feature in our ensemble solutions as additional data constraints are added to the inversion, justifying more complex solutions. The low-viscosity region is a pronounced feature in the viscosity profiles based on ME16-160 and there also appears to be a more subtle expression of this feature in the viscosity profiles based on SEMUCB-WM1. Such a feature has been suggested on the basis of several lines of evidence. First, the transition from ringwoodite to bridgmanite plus ferropericlasite involves complete recrystallization of the dominant phases present, and multiple mechanisms associated with the phase transition could modify the viscosity. In convective downwellings, the phase transition could be accompanied by a dramatic reduction in grain size to  $\sim\mu\text{m}$  size (*Solomatov and Reese*, 2008). On theoretical grounds, it might be expected that transformational superplasticity could reduce viscosity

by two to three orders of magnitude within 1.5 km of the 650 km phase transition (Panasyuk and Hager, 1998). Second, inversions for the viscosity profile constrained by the global long-wavelength geoid allowed for the presence of a low-viscosity channel at the base of the upper mantle (Forte et al., 1993), and a similar “second asthenosphere” was recovered in inversions constrained by regional (oceanic) geoid anomalies (Kido et al., 1998). The effect of the low-viscosity channel can modify predictions associated with GIA observables Milne et al. (1998), and in joint inversions of GIA, misfits can be significantly reduced for models that include such a low-viscosity notch (Mitrovica and Forte, 2004). Finally, in global geodynamic models with prescribed plate motions, the behavior of slabs is broadly consistent with observations of stagnation when such a feature is included (Mao and Zhong, 2018; Lourenço and Rudolph, in review).

An increase in viscosity in the mid-mantle or viscosity “hill,” which is a feature common to all of our viscosity inversions, has been suggested on the basis of geophysical inversions, and several potential mechanisms exist to explain such a feature. An increase in viscosity below 650 km depth has been recovered in many inversions constrained by the long wavelength geoid and GIA observables (e.g., King and Masters, 1992; Mitrovica and Forte, 1997; Forte and Mitrovica, 2001; Rudolph et al., 2015). An increase in viscosity would be expected to slow sinking slabs (Morra et al., 2010) and affect the dynamics of plumes. The correlation between subduction history and tomographic models has been used to test whether slabs sink at a uniform rate in the lower mantle. A recent study of the similarity between convergence patterns in plate reconstructions and patterns of mantle lateral heterogeneity from an average of  $V_S$  tomographic models suggests that the data can neither confirm nor reject the possibility of a change in viscosity below 600 km (Domeier et al., 2016). On the other hand, an analysis of a catalog that relates imaged fast anomalies to specific subduction events does find evidence that the rate of slab sinking decreases across a “slab deceleration zone” between 650–1500 km (van der Meer et al., 2018); one explanation for such a deceleration zone is the increase in viscosity in the shallow lower mantle seen in all of our inverted viscosity profiles.

Several mechanisms exist that could produce an increase in viscosity in the mid-mantle. Marquardt and Miyagi (2015) measured the strength of ferropericlase at pressures of 20–60 GPa (600–1,000 km) and observed an increase in strength across this range of pressures. Though ferropericlase is a minor modal component of the lower mantle, it could become rheologically limiting if organized into sheets within rapidly deforming regions, an idea supported by experiments with two-phase analog materials (Kaercher et al., 2016) and with bridgmanite-

magnesiowüstite mixtures (Girard et al., 2016). If the lower mantle rheology is determined by the arrangement of distinct mineral phases, we expect history-dependence and anisotropy of viscosity (Thielmann et al., 2020), further confounding our interpretations of viscosity in inversions. An increase in the viscosity of ferropericlase is also supported by experimental determinations of the melting temperature at mantle pressures (Deng and Lee, 2017), which show a local maximum in melting temperature for pressures near 40 GPa (1,000 km). Changes in the proportionation of iron could also alter the viscosity of bridgmanite across a depth range consistent with the inferred mid-mantle viscosity increase. Shim et al. (2017) suggested that at depths of 1,100–1,700 km, an increase in the proportionation of iron into ferropericlase could depress the melting point of bridgmanite, increasing the viscosity predicted using homologous temperature scaling. These various mechanisms are not mutually exclusive and could operate in concert to produce an increase in viscosity near 1,000 km. Finally, we note that the deformation mechanisms of even single phases within the lower mantle remain uncertain. While the lower mantle has long been thought to deform by diffusion creep due to absence of seismic anisotropy at most lower mantle depths, recent calculations suggest that another deformation mechanism – pure climb creep, which is insensitive to grain size and produces no seismic anisotropy – may be active in bridgmanite at lower mantle conditions (Boioli et al., 2017).

## 1.5. CONCLUSIONS

We analyzed the long-wavelength structure of four recent global tomographic models and compared the features of these models with predicted structures in five geodynamic models that incorporate surface velocity constraints from plate reconstructions. The long-wavelength radial correlation functions of SEMUCB-WM1 and SEISGLOB2 show strong evidence for a change in radial correlation structure near 1,000 km depth, whereas the most abrupt change in the RCFs for S362ANI+M and GLAD-M15 occur at 650 km depth. The change in the RCF reflects a change in the pattern of long-wavelength structure between the lower mantle and transition zone. The transition zone structure is correlated with more recent subduction history, whereas the long-wavelength, lower-mantle structure is more similar to ancient subduction history, in agreement with previous work. The long-wavelength transition zone structure is dominated by seismically fast anomalies in the Western Pacific, and especially beneath the Philippine Sea Plate. This suggests that the change in the pattern of long-wavelength heterogeneity in the transition zone and shallow lower mantle is

controlled by subduction history and by the interaction of slabs with mantle phase transitions and rheological changes. The depth of changes in the pattern of heterogeneity in the models (and the associated RCFs) is sensitive to the data used to constrain the inversions and the radial parameterizations. Future studies that investigate whether these changes in long-wavelength structure occur at 650 km depth or somewhat deeper within the lower mantle will have important implications for our understanding of mantle structure and dynamics. All of the tomographic models show a local minimum in the spectral slope at or slightly above 650 km, indicating concentration of power at longer wavelengths within the transition zone. This feature is most consistent with a global geodynamic model that includes a weakly endothermic ( $-2$  MPa/K) phase transition at 660 km depth and a low viscosity channel below 660 km and a viscosity increase in the shallow lower mantle. New inferences of the viscosity profile (Figure 1.6) using both a whole-mantle density model from full-spectrum tomography (Moulik and Ekström, 2016) and a scaled  $V_S$  model (SEMUCB-WM1, French and Romanowicz (2014)), recover viscosity profiles that are compatible with the presence of a low-viscosity channel below 660 km depth and a viscosity maximum in the mid-mantle.

## ACKNOWLEDGMENTS

The authors thank John Hernlund and Fred Richards for their reviews, which improved the quality and clarity of the manuscript. The authors thank Ebru Bozdağ for providing the GLAD-M15 tomographic model and for helpful discussions about this model. All of the authors acknowledge support from the National Science Foundation through NSF Geophysics grant EAR-1825104, and MLR acknowledges NSF CSEDI grant EAR-1800450. Computational resources were provided through NSF Major Research Instrumentation grant DMS-1624776 to Portland State University and by UC Davis. VL acknowledges support from the Packard Foundation.

## REFERENCES

- Austermann, J., B. T. Kaye, J. X. Mitrovica, & P. Huybers (2014). A statistical analysis of the correlation between large igneous provinces and lower mantle seismic structure. *Geophysical Journal International*, *197*(1), 1–9, doi:10.1093/gji/ggt500.
- Ballmer, M. D., N. C. Schmerr, T. Nakagawa, & J. Ritsema (2015). Compositional mantle layering revealed by slab stagnation at  $\sim 1000$ -km depth. *Science Advances*, *1*(11), e1500815, doi:10.1126/sciadv.1500815.
- Becker, T. W., & L. Boschi (2002). A comparison of tomographic and geodynamic mantle models. *Geochemistry, Geophysics, Geosystems*, *3*(1), 1003–n/a, doi:10.1029/2001GC000168.
- Becker, T. W., C. O'Neill, & B. Steinberger (2014). HC, a global mantle circulation solver.
- Boioli, F., P. Carrez, P. Cordier, B. Devincere, K. Gouriet, P. Hirel, A. Kraych, & S. Ritterbex (2017). Pure climb creep mechanism drives flow in Earth's lower mantle. *Science Advances*, *3*(3), e1601958, doi:10.1126/sciadv.1601958.
- Boschi, L., & A. M. Dziewonski (1999). High- and low-resolution images of the Earth's mantle: Implications of different approaches to tomographic modeling. *Journal of Geophysical Research: Solid Earth*, *104*(B11), 25,567–25,594, doi:10.1029/1999JB900166.
- Bower, D. J., M. Gurnis, & M. Seton (2013). Lower mantle structure from paleogeographically constrained dynamic Earth models. *Geochemistry, Geophysics, Geosystems*, *14*(1), 44–63, doi:10.1029/2012GC004267.
- Bozdağ, E., D. Peter, M. Lefebvre, D. Komatitsch, J. Tromp, J. Hill, N. Podhorszki, & D. Pugmire (2016). Global adjoint tomography: first-generation model. *Geophysical Journal International*, *207*(3), 1739–1766, doi:10.1093/gji/ggw356.
- Burke, K., & T. H. Torsvik (2004). Derivation of Large Igneous Provinces of the past 200 million years from long-term heterogeneities in the deep mantle. *Earth and Planetary Science Letters*, *227*(3–4), 531–538.
- Burke, K., B. Steinberger, T. H. Torsvik, & M. A. Smethurst (2008). Plume Generation Zones at the margins of Large Low Shear Velocity Provinces on the core–mantle boundary. *Earth and Planetary Science Letters*, *265*(1–2), 49–60, doi:10.1016/j.epsl.2007.09.042.
- Cammarano, F., S. Goes, P. Vacher, & D. Giardini (2003). Inferring upper-mantle temperatures from seismic velocities. *Physics of the Earth and Planetary Interiors*, *138*(3), 197–222, doi:10.1016/S0031-9201(03)00156-0.
- Capdeville, Y., Y. Gung, & B. Romanowicz (2005). Towards global earth tomography using the spectral element method: a technique based on source stacking. *Geophysical Journal International*, *162*(2), 541–554, doi:10.1111/j.1365-246X.2005.02689.x.
- Chambat, F., Y. Ricard, & B. Valette (2010). Flattening of the Earth: further from hydrostaticity than previously estimated. *Geophysical Journal International*, *183*(2), 727–732, doi:10.1111/j.1365-246X.2010.04771.x.
- Christensen, U. R., & D. A. Yuen (1985). Layered convection induced by phase transitions. *Journal of Geophysical Research: Solid Earth*, *90*(B12), 10,291–10,300, doi:10.1029/JB090iB12p10291.
- Conrad, C. P., B. Steinberger, & T. H. Torsvik (2013). Stability of active mantle upwelling revealed by net characteristics of plate tectonics. *Nature*, *498*(7455), 479–482, doi:10.1038/nature12203.
- Cottaar, S., & V. Lekic (2016). Morphology of seismically slow lower-mantle structures. *Geophysical Journal International*, *207*(2), 1122–1136, doi:10.1093/gji/ggw324.
- Dahlen, F. A., & J. Tromp (1998). *Theoretical Global Seismology*, Princeton University Press.

- Davaille, A., F. Girard, & M. Le Bars (2002), How to anchor hotspots in a convecting mantle? *Earth and Planetary Science Letters*, 203(2), 621–634, doi:10.1016/S0012-821X(02)00897-X.
- Davies, D. R., S. Goes, & H. C. P. Lau (2015), Thermally Dominated Deep Mantle LLSVPs: A Review. In A. Khan and F. Deschamps (Eds.), *The Earth's Heterogeneous Mantle: A Geophysical, Geodynamical, and Geochemical Perspective*, pp. 441–477, Springer International Publishing, Cham, doi:10.1007/978-3-319-15627-9\_14.
- Deng, J., & K. K. M. Lee (2017), Viscosity jump in the lower mantle inferred from melting curves of ferropicriase. *Nature Communications*, 8(1), 1997, doi:10.1038/s41467-017-02263-z.
- Domeier, M., P. V. Doubrovine, T. H. Torsvik, W. Spakman, & A. L. Bull (2016), Global correlation of lower mantle structure and past subduction. *Geophysical Research Letters*, 43(10), 4945–4953, doi:10.1002/2016GL068827.
- Durand, S., E. Debayle, Y. Ricard, C. Zaroli, & S. Lambotte (2017), Confirmation of a change in the global shear velocity pattern at around 1000 km depth. *Geophysical Journal International*, 211(3), 1628–1639, doi:10.1093/gji/ggx405.
- Fei, Y., J. Van Orman, J. Li, W. van Westrenen, C. Sanloup, W. Minarik, K. Hirose, T. Komabayashi, M. Walter, & K. Funakoshi (2004), Experimentally determined postspinel transformation boundary in Mg<sub>2</sub>SiO<sub>4</sub> using MgO as an internal pressure standard and its geophysical implications. *Journal of Geophysical Research: Solid Earth (1978–2012)*, 109(B2).
- Forte, A. M., & J. X. Mitrovica (2001), Deep-mantle high-viscosity flow and thermochemical structure inferred from seismic and geodynamic data. *Nature*, 410, 1049–1056.
- Forte, A. M., A. M. Dziewonski, & R. L. Woodward (1993), Aspherical Structure of the Mantle, Tectonic Plate Motions, Nonhydrostatic Geoid, and Topography of the Core-Mantle Boundary. In *Dynamics of Earth's Deep Interior and Earth Rotation*, pp. 135–166, American Geophysical Union (AGU), doi:10.1029/GM072p0135.
- French, S. W., & B. Romanowicz (2015), Broad plumes rooted at the base of the Earth's mantle beneath major hotspots. *Nature*, 525(7567), 95–99, doi:10.1038/nature14876.
- French, S. W., & B. A. Romanowicz (2014), Whole-mantle radially anisotropic shear velocity structure from spectral-element waveform tomography. *Geophysical Journal International*, 199(3), 1303–1327, doi:10.1093/gji/ggu334.
- Frost, D. A., E. J. Garnero, & S. Rost (2018), Dynamical links between small- and large-scale mantle heterogeneity: Seismological evidence. *Earth and Planetary Science Letters*, 482, 135–146, doi:10.1016/j.epsl.2017.10.058.
- Fukao, Y., & M. Obayashi (2013), Subducted slabs stagnant above, penetrating through, and trapped below the 660 km discontinuity. *Journal of Geophysical Research (Solid Earth)*, 118(11), 2013JB010466–5938, doi:10.1002/2013JB010466.
- Ghosh, A., T. W. Becker, & S. J. Zhong (2010), Effects of lateral viscosity variations on the geoid. *Geophysical Research Letters*, 37(1), 01,301, doi:10.1029/2009GL040426.
- Girard, J., G. Amulele, R. Farla, A. Mohiuddin, and S.-i. Karato (2016), Shear deformation of bridgmanite and magnesiowüstite aggregates at lower mantle conditions. *Science*, 351(6269), 144–147, doi:10.1126/science.aad3113.
- Green, P. J. (1995), Reversible jump Markov chain Monte Carlo computation and Bayesian model determination. *Biometrika*, 82(4), 711–732, doi:10.1093/biomet/82.4.711.
- Hager, B. H., & R. J. O'Connell (1981), A simple global model of plate dynamics and mantle convection. *Journal of Geophysical Research*, 86(B), 4843–4867, doi:10.1029/JB086iB06p04843.
- Hager, B. H., R. W. Clayton, M. A. Richards, R. P. Comer, & A. M. Dziewonski (1985), Lower mantle heterogeneity, dynamic topography and the geoid. *Nature*, 313(6003), 541–545, doi:10.1038/314752a0.
- He, Y., & L. Wen (2009), Structural features and shear-velocity structure of the “Pacific Anomaly.” *J. Geophys. Res.*, 114(B2), B02,309, doi:10.1029/2008JB005814.
- Jellinek, A. M., & M. Manga (2002), The influence of a chemical boundary layer on the fixity, spacing and lifetime of mantle plumes. *Nature*, 418(6899), 760–763, doi:10.1038/nature00979.
- Jenkins, J., A. Deuss, & S. Cottaar (2016), Converted phases from sharp 1000 km depth mid-mantle heterogeneity beneath Western Europe. *Earth and Planetary Science Letters*, 459, 196–207, doi:10.1016/j.epsl.2016.11.031.
- Jordan, T. H., P. Puster, & G. A. Glatzmaier (1993), Comparisons between seismic Earth structures and mantle flow models based on radial correlation functions. *Science*, 261, 1427–1431.
- Kaercher, P., L. Miyagi, W. Kaniitpanyacharoen, E. Zepeda-Alarcon, Y. Wang, D. Parkinson, R. A. Lebensohn, F. De Carlo, & H.-R. Wenk (2016), Two-phase deformation of lower mantle mineral analogs. *Earth and Planetary Science Letters*, 456, 134–145, doi:10.1016/j.epsl.2016.09.030.
- Karato, S.-i., & B. B. Karki (2001), Origin of lateral variation of seismic wave velocities and density in the deep mantle. *Journal of Geophysical Research: Solid Earth*, 106(B10), 21,771–21,783, doi:10.1029/2001JB000214.
- Katsura, T., H. Yamada, T. Shinmei, A. Kubo, S. Ono, M. Kanzaki, A. Yoneda, M. J. Walter, E. Ito, S. Urakawa, K. Funakoshi, & W. Utsumi (2003), Post-spinel transition in Mg<sub>2</sub>SiO<sub>4</sub> determined by high P–T in situ X-ray diffractometry. *Physics of the Earth and Planetary Interiors*, 136(1–2), 11–24.
- Kido, M., D. A. Yuen, O. Čadež, & T. Nakakuki (1998), Mantle viscosity derived by genetic algorithm using oceanic geoid and seismic tomography for whole-mantle versus blocked-flow situations. *Physics of the Earth and Planetary Interiors*, 107(4), 307–326.
- King, S. D., & G. Masters (1992), An inversion for radial viscosity structure using seismic tomography. *Geophysical Research Letters*, 19(15), 1551–1554, doi:10.1029/92GL01700.
- Komatitsch, D., & J. Tromp (2002), Spectral-element simulations of global seismic wave propagation—I. Validation. *Geophysical Journal International*, 149(2), 390–412, doi:10.1046/j.1365-246X.2002.01653.x.
- Kustowski, B., G. Ekström, & A. M. Dziewoński (2008), Anisotropic shear-wave velocity structure of the Earth's mantle: A global model. *Journal of Geophysical Research: Solid Earth*, 113(B6), doi:10.1029/2007JB005169.
- Lau, H. C. P., J. X. Mitrovica, J. Austermann, O. Crawford, D. Al-Attar, & K. Letychev (2016), Inferences of mantle viscosity based on ice age data sets: Radial structure. *Journal of*

- Geophysical Research*, 123, 7237–7252, doi:https://doi.org/10.1029/2018JB015740.
- Lau, H. C. P., J. X. Mitrovica, J. L. Davis, J. Tromp, H.-Y. Yang, & D. Al-Attar (2017). Tidal tomography constrains Earth's deep-mantle buoyancy. *Nature*, 551, 321–326, doi:10.1038/nature24452.
- Li, X.-D., & B. Romanowicz (1995). Comparison of global waveform inversions with and without considering cross-branch modal coupling. *Geophysical Journal International*, 121(3), 695–709, doi:10.1111/j.1365-246X.1995.tb06432.x.
- Liu, X., & S. Zhong (2015). The long-wavelength geoid from three-dimensional spherical models of thermal and thermochemical mantle convection. *Journal of Geophysical Research: Solid Earth*, 120(6), 4572–4596, doi:10.1002/2015JB012016.
- Liu, X., & S. Zhong (2016). Constraining mantle viscosity structure for a thermochemical mantle using the geoid observation. *Geochemistry, Geophysics, Geosystems*, 17(3), 895–913, doi:10.1002/2015GC006161.
- Lourenço, D. L., & M. L. Rudolph (in review). Shallow lower mantle viscosity modulates the pattern of mantle structure, in review at *Proceedings of the National Academy of Sciences*.
- Malinverno, A. (2002). Parsimonious Bayesian Markov chain Monte Carlo inversion in a nonlinear geophysical problem. *Geophysical Journal International*, 151(3), 675–688, doi:10.1046/j.1365-246X.2002.01847.x.
- Malinverno, A., & V. A. Briggs (2004). Expanded uncertainty quantification in inverse problems: Hierarchical Bayes and empirical Bayes. *Geophysics*, 69(4), 1005–1016, doi:10.1190/1.1778243.
- Mao, W., & S. Zhong (2018). Slab stagnation due to a reduced viscosity layer beneath the mantle transition zone. *Nature Geoscience*, 11(11), 876, doi:10.1038/s41561-018-0225-2.
- Mao, W., & S. Zhong (2019). Controls on global mantle convective structures and their comparison with seismic models. *Journal of Geophysical Research: Solid Earth*, doi:10.1029/2019JB017918.
- Marquardt, H., & L. Miyagi (2015). Slab stagnation in the shallow lower mantle linked to an increase in mantle viscosity. *Nature Geoscience*, 8(4), 311–314, doi:10.1038/ngeo2393.
- Masters, G., S. Johnson, G. Laske, H. Bolton, & J. H. Davies (1996). A Shear-Velocity Model of the Mantle [and Discussion]. *Philosophical Transactions of the Royal Society of London. Series A: Mathematical, Physical and Engineering Sciences*, 354(1711), 1385–1411, doi:10.1098/rsta.1996.0054.
- Masters, G., G. Laske, H. Bolton, & A. Dziewonski (2000). The Relative Behavior of Shear Velocity, Bulk Sound Speed, and Compressional Velocity in the Mantle: Implications for Chemical and Thermal Structure. In *Earth's Deep Interior: Mineral Physics and Tomography From the Atomic to the Global Scale*, vol. 117, edited by S.-i. Karato, A. M. Forte, R. Lieberman, G. Masters, & L. Stixrude, pp. 63–87, American Geophysical Union, Washington, D. C.
- Matthews, K. J., K. T. Maloney, S. Zahirovic, S. E. Williams, M. Seton, & R. D. Müller (2016). Global plate boundary evolution and kinematics since the late Paleozoic. *Global and Planetary Change*, 146, 226–250, doi:10.1016/j.gloplacha.2016.10.002.
- McNamara, A. K., & S. Zhong (2004). Thermochemical structures within a spherical mantle: Superplumes or piles? *J. Geophys. Res.*, 109(B7), B07402, doi:10.1029/2003JB002847.
- McNamara, A. K., & S. Zhong (2005). Thermochemical structures beneath Africa and the Pacific Ocean. *Nature*, 437(7062), 1136–1139, doi:10.1038/nature04066.
- Milne, G. A., J. X. Mitrovica, & A. M. Forte (1998). The sensitivity of glacial isostatic adjustment predictions to a low-viscosity layer at the base of the upper mantle. *Earth and Planetary Science Letters*, 154(1), 265–278, doi:10.1016/S0012-821X(97)00191-X.
- Mitrovica, J. X., & A. M. Forte (1997). Radial profile of mantle viscosity: Results from the joint inversion of convection and postglacial rebound observables. *Journal of Geophysical Research: Solid Earth*, 102(B2), 2751–2769, doi:10.1029/96JB03175.
- Mitrovica, J. X., & A. M. Forte (2004). A new inference of mantle viscosity based upon joint inversion of convection and glacial isostatic adjustment data. *Earth and Planetary Science Letters*, 225(1–2), 177–189, doi:10.1016/j.epsl.2004.06.005.
- Morra, G., D. A. Yuen, L. Boschi, P. Chatelain, P. Koumoutsakos, & P. J. Tackley (2010). The fate of the slabs interacting with a density/viscosity hill in the mid-mantle. *Physics of the Earth and Planetary Interiors*, 180(3–4), 271–282, doi:10.1016/j.pepi.2010.04.001.
- Moulik, P., & G. Ekström (2014). An anisotropic shear velocity model of the Earth's mantle using normal modes, body waves, surface waves and long-period waveforms. *Geophysical Journal International*, 199(3), 1713–1738, doi:10.1093/gji/ggu356.
- Moulik, P., & G. Ekström (2016). The relationships between large-scale variations in shear velocity, density, and compressional velocity in the Earth's mantle. *Journal of Geophysical Research (Solid Earth)*, 121(4), 2737–2771, doi:10.1002/2015JB012679.
- Mégnin, C., H.-P. Bunge, B. Romanowicz, & M. A. Richards (1997). Imaging 3-D spherical convection models: What can seismic tomography tell us about mantle dynamics? *Geophysical Research Letters*, 24(11), 1299–1302, doi:10.1029/97GL01256.
- Nelson, P. L., & S. P. Grand (2018). Lower-mantle plume beneath the Yellowstone hotspot revealed by core waves. *Nature Geoscience*, 11(4), 280–284, doi:10.1038/s41561-018-0075-y.
- Obayashi, M., J. Yoshimitsu, G. Nolet, Y. Fukao, H. Shiobara, H. Sugioka, H. Miyamachi, & Y. Gao (2013). Finite frequency whole mantle *P* wave tomography: Improvement of subducted slab images. *Geophysical Research Letters*, 40(21), 2013GL057401–5657, doi:10.1002/2013GL057401.
- Panasjuk, S. V., & B. H. Hager (1998). A model of transformational superplasticity in the upper mantle. *Geophysical Journal International*, 133(3), 741–755, doi:10.1046/j.1365-246X.1998.00539.x.
- Puster, P., & T. H. Jordan (1994). Stochastic analysis of mantle convection experiments using two-point correlation functions. *Geophysical Research Letters*, 21(4), 305–308, doi:10.1029/93GL02934.
- Puster, P., T. H. Jordan, & B. H. Hager (1995). Characterization of mantle convection experiments using two-point correlation

- functions. *Journal of Geophysical Research: Solid Earth*, 100 (B4), 6351–6365, doi:10.1029/94JB03268.
- Ricard, Y., M. Richards, C. Lithgow-Bertelloni, & Y. Le Stunff (1993). A geodynamic model of mantle density heterogeneity. *J. Geophys. Res.*, 98(B12), 21,895, doi:10.1029/93JB02216.
- Richards, M. A., & B. H. Hager (1984). Geoid anomalies in a dynamic Earth. *Journal of Geophysical Research: Solid Earth*, 89(B7), 5987–6002, doi:10.1029/JB089iB07p05987.
- Richards, M. A., & B. H. Hager (1989). Effects of lateral viscosity variations on long-wavelength geoid anomalies and topography. *J. Geophys. Res.*, 94(B8), 10,299, doi:10.1029/JB094iB08p10299.
- Rickers, F., A. Fichtner, & J. Trampert (2013). The Iceland-Jan Mayen plume system and its impact on mantle dynamics in the North Atlantic region: Evidence from full-waveform inversion. *Earth and Planetary Science Letters*, 367, 39–51.
- Ries, J., S. Bettadpur, R. Eanes, Z. Kang, U. Ko, C. McCullough, P. Nagel, N. Pie, S. Poole, T. Richter, H. Save, & B. Tapley (2016). Development and Evaluation of the Global Gravity Model GGM05. *Tech. Rep. CSR-16-02*, The University of Texas at Austin, Center for Space Research.
- Rudolph, M. L., & S. Zhong (2013). Does quadrupole stability imply LLSVP fixity? *Nature*, 503(7477), E3–E4, doi:doi:10.1038/nature12792.
- Rudolph, M. L., & S. J. Zhong (2014). History and dynamics of net rotation of the mantle and lithosphere. *Geochemistry, Geophysics, Geosystems*, 15(9), 3645–3657.
- Rudolph, M. L., V. Lekic, & C. Lithgow-Bertelloni (2015). Viscosity jump in Earth's mid-mantle. *Science*, 350(6266), 1349–1352, doi:10.1126/science.aad1929.
- Sambridge, M., T. Bodin, K. Gallagher, & H. Tkalcic (2013). Transdimensional inference in the geosciences. *Philosophical Transactions of the Royal Society A: Mathematical, Physical and Engineering Sciences*, 371, 20110,547, doi:10.1111/j.1365-246X.1990.tb04588.x.
- Schuberth, B. S. A., H.-P. Bunge, & J. Ritsema (2009). Tomographic filtering of high-resolution mantle circulation models: Can seismic heterogeneity be explained by temperature alone? *Geochemistry, Geophysics, Geosystems*, 10(5), doi:10.1029/2009GC002401.
- Shim, S.-H., B. Grocholski, Y. Ye, E. E. Alp, S. Xu, D. Morgan, Y. Meng, & V. B. Prakapenka (2017). Stability of ferrous-iron-rich bridgmanite under reducing midmantle conditions. *Proceedings of the National Academy of Sciences*, 114(25), 6468–6473, doi:10.1073/pnas.1614036114.
- Simons, F., F. Dahlen, & M. Wieczorek (2006). Spatospectral Concentration on a Sphere. *SIAM Review*, 48(3), 504–536, doi:10.1137/S0036144504445765.
- Solomatov, V. S., & C. C. Reese (2008). Grain size variations in the Earth's mantle and the evolution of primordial chemical heterogeneities. *Journal of Geophysical Research: Solid Earth*, 113(B7), doi:10.1029/2007JB005319.
- Steinberger, B., & R. Holme (2008). Mantle flow models with core-mantle boundary constraints and chemical heterogeneities in the lowermost mantle. *Journal of Geophysical Research: Solid Earth*, 113(B5), doi:10.1029/2007JB005080.
- Stixrude, L., & C. Lithgow-Bertelloni (2011). Thermodynamics of mantle minerals - II. Phase equilibria. *Geophysical Journal International*, 184(3), 1180–1213, doi:10.1111/j.1365-246X.2010.04890.x.
- Su, W.-j., & A. M. Dziewonski (1991). Predominance of long-wavelength heterogeneity in the mantle. *Nature*, 352(6331), 121–126, doi:10.1038/352121a0.
- Su, W.-j., & A. M. Dziewonski (1992). On the scale of mantle heterogeneity. *Physics of the Earth and Planetary Interiors*, 74(1), 29–54, doi:10.1016/0031-9201(92)90066-5.
- Su, W.-j., & A. M. Dziewonski (1997). Simultaneous inversion for 3-D variations in shear and bulk velocity in the mantle. *Physics of the Earth and Planetary Interiors*, 100(1–4), 135–156.
- Thielmann, M., G. J. Golabek, & H. Marquardt (2020). Ferropericlasite control of lower mantle rheology: Impact of phase morphology. *Geochemistry, Geophysics, Geosystems*, (n/a), doi:10.1029/2019GC008688.
- Thorne, M. S., E. J. Garnero, & S. P. Grand (2004). Geographic correlation between hot spots and deep mantle lateral shear-wave velocity gradients. *Physics of the Earth and Planetary Interiors*, 146(1–2), 47–63, doi:10.1016/j.pepi.2003.09.026.
- Torsvik, T. H., M. A. Smethurst, K. Burke, & B. Steinberger (2006). Large igneous provinces generated from the margins of the large low-velocity provinces in the deep mantle. *Geophysical Journal International*, 167(3), 1447–1460, doi:10.1111/j.1365-246X.2006.03158.x.
- van der Meer, D. G., D. J. J. van Hinsbergen, & W. Spakman (2018). Atlas of the underworld: Slab remnants in the mantle, their sinking history, and a new outlook on lower mantle viscosity. *Tectonophysics*, 723, 309–448, doi:10.1016/j.tecto.2017.10.004.
- Wang, Y., & L. Wen (2007). Geometry and P and S velocity structure of the “African Anomaly.” *J. Geophys. Res.*, 112(B5), B05,313, doi:10.1029/2006JB004483.
- Waszek, L., N. C. Schmerr, & M. D. Ballmer (2018). Global observations of reflectors in the mid-mantle with implications for mantle structure and dynamics. *Nature Communications*, 9(1), 1–13, doi:10.1038/s41467-017-02709-4.
- Wen, L., & D. L. Anderson (1995). The fate of slabs inferred from seismic tomography and 130 million years of subduction. *Earth and Planetary Science Letters*, 133(1), 185–198, doi:10.1016/0012-821X(95)00064-J.
- Williams, C. D., S. Mukhopadhyay, M. L. Rudolph, & B. Romanowicz (2019). Primitive Helium is Sourced from Seismically Slow Regions in the Lowermost Mantle. *Geochemistry, Geophysics, Geosystems*, 20(8), 4130–4145, doi:10.1029/2019GC008437.
- Yuan, K., & B. Romanowicz (2017). Seismic evidence for partial melting at the root of major hot spot plumes. *Science*, 357(6349), 393–397, doi:10.1126/science.aan0760.
- Zhang, N., S. Zhong, W. Leng, & Z.-X. Li (2010). A model for the evolution of the Earth's mantle structure since the Early Paleozoic. *J. Geophys. Res.*, 115(B6), B06,401, doi:10.1029/2009JB006896.
- Zhong, S., M. T. Zuber, L. Moresi, & M. Gurnis (2000). Role of temperature-dependent viscosity and surface plates in spherical shell models of mantle convection. *J. Geophys. Res.*, 105(B5), 11,063–11,082, doi:10.1029/2000JB900003.
- Zhong, S., A. McNamara, E. Tan, L. Moresi, & M. Gurnis (2008). A benchmark study on mantle convection in a 3-D spherical shell using CitcomS. *Geochemistry, Geophysics, Geosystems*, 9(10), Q10,017.